Journal of Materials Chemistry A

PAPER

View Article Online
View Journal | View Issue



Cite this: J. Mater. Chem. A, 2016, 4, 18100

# Highly active Co–Mo–C/NRGO composite as an efficient oxygen electrode for water–oxygen redox cycle†

Chun-Hui Liu,‡ Yu-Jia Tang,‡ Xiao-Li Wang, Wei Huang, Shun-Li Li,* Long-Zhang Dong and Ya-Qian Lan*

Received 14th September 2016
Accepted 21st October 2016

DOI: 10.1039/c6ta07952k

www.rsc.org/MaterialsA

The slow kinetics of the oxygen evolution reaction (OER) and the oxygen reduction reaction (ORR) have hindered energy conversion and storage greatly. Design of a new class of low-cost and highly efficient electrocatalysts for the water–oxygen redox cycle (WORC) system including OER and ORR is considered a huge challenge. Controlled synthesis of unique and stable precursors as a perfect platform to synthesize target products with diverse compositions are of vital importance. Herein, we synthesized a metal/metal carbide-based composite (denoted as Co–Mo–C/NRGO-1) by directly carbonizing Co-doped polyoxometalate/conductive polymer/graphene precursor (Co-PCG) as an efficient bi-functional electrocatalyst. The resulting Co–Mo–C/NRGO-1 composite exhibited superior electrocatalytic activity for OER with an ultra-low Tafel slope of 42 mV $dec^{-1}$, a small overpotential of 330 mV *vs.* RHE at the current density of 10 mA $cm^{-2}$ and long-term stability in alkaline medium. The ORR performance was also investigated with a positive onset potential (~−95 mV *vs.* Ag/AgCl), remarkable stability over 30 000 s and good tolerance to methanol crossover. Most importantly, the OER performance of Co–Mo–C/NRGO-1 was the best among all the reported carbide-based materials and was comparable to the best OER electrodes.

With the increasing demand for energy and severe damage to the environment due to fossil fuels, it is extremely urgent to develop efficient technology for producing clean and sustainable energies.[1,2] The water–oxygen redox cycle (WORC) system[3] including both oxygen evolution reaction (OER) and oxygen reduction reaction (ORR) is considered to be a pivotal technology for several energy conversion systems, including fuel cells[4] and water splitting.[5,6] The WORC system can be a highly efficient energy-saving project that works as ORR consumes oxygen ($O_2$) and in converse has water splitting that produces $O_2$. Commercial iridium oxides ($IrO_2$) and platinum (Pt) have been generally considered as the most active electrocatalysts for OER and ORR, respectively.[7,8] However, these noble-based catalysts still have high costs, limited supply and degraded catalytic performance over time, which hinders their industrial applications. Therefore, great efforts should be made towards rational design of non-noble metal electrocatalysts as alternatives for boosting the WORC system dramatically. Only in recent years, researches of bi-functional electrocatalysts for both OER and ORR have seen success, however great challenges still exist and need further exploitation because of their limited activity and stability.[9–14]

Transition metal carbides (TMCs), which can be synthesized mostly by the temperature programmed reduction (TPR) method, have received attention as effective electrocatalysts because of the high stability and durability in strong acid or alkaline medium.[15–17] However, almost all of the reported TMCs-based materials have been used as excellent hydrogen evolution reaction (HER) electrocatalysts with few studies as OER electrocatalysts, which impeded the development of TMCs in water splitting.[18–21] Thus, it is a very imperative subject to improve the OER activity of TMCs-based materials. Furthermore, introducing a second transition metal to fine-tune the crystal structure of carbides can evidently improve the electrocatalytic activity for the obtained bimetallic carbide-based materials.[22–24] Graphene-based composites have been extensively proposed and reported as robust electrocatalysts currently because the introduction of graphene can improve the conductivity and provide optimized electronic structures.[11,25,26] Therefore, hybridizing bimetallic carbides with graphene films to synthesize bimetallic carbides and graphene-based materials is a feasible strategy for further improving the OER performance. However, such a system containing carbides and graphene appears to be very complicated due to the diversity of the

*Jiangsu Key Laboratory of Biofunctional Materials, School of Chemistry and Materials Science, Nanjing Normal University, Nanjing 210023, Jiangsu, P. R. China. E-mail: yqlan@njnu.edu.cn; slli@njnu.edu.cn*

† Electronic supplementary information (ESI) available: Experimental details, PXRD patterns, TEM and SEM images, XPS, Raman. See DOI: 10.1039/c6ta07952k

‡ These authors contributed equally.

sample compositions, which might be prepared through several complex experimental procedures and often have disorder and agglomerate morphologies. Inspired by this, we attempted to adopt a simple and convenient experimental method to synthesize a stable precursor with uniform structures, and then carbonized it directly to obtain carbide-based materials easily by the TPR method. Thus, the technique adopted for the preparation of stable and uniform precursors is very crucial and can directly determine the structure and chemical properties of the precursors-derived materials.

On the basis of our previous reports, we have chosen the polyoxometalate/conductive polymer/graphene system (denoted as PCG) as an ideal platform for the preparation of stable precursors.[27,28] Interestingly, the PCG system possesses unique structures, excellent conductivity and considerable carbon sources because of the combination with conductive polymer and graphene films, which can be prepared abundantly through a simple one-step stirring or hydrothermal method. In addition, modifying PCG system with another transition metal doping (denoted as metal-PCG) not only still retains the morphology and structure of PCG, but also enables the PCG system to be studied as precursors more efficiently. In that sense, metal-PCG precursor, as a perfect platform, makes sure that the preparation of metal-PCG derived nanocomposites with complicated compositions, but distinct structures occurs handily and saves the trouble of a multi-step synthesis process.

In this study, a metal-PCG system as precursor was chosen to carbonize directly to synthesize bimetallic carbides and graphene-based composites with the TPR method. First, $PMo_{12}$, a type of common POMs, pyrrole monomer (Py), graphene oxide (GO) and cobalt nitrate ($Co(NO_3)_2$) were chosen as the precursors to synthesize Co-PCG system by a one-pot hydrothermal method. Then, nitrogen-doped reduced graphene oxide-supported metal cobalt (Co), bimetallic interstitial carbide ($Co_6Mo_6C_2$) and molybdenum carbide ($Mo_2C$) composite (denote as Co–Mo–C/NRGO-1) was synthesized by direct carbonization of the Co-PCG system. Due to the good water-solubility, both $PMo_{12}$ and $Co^{2+}$ ions could disperse in graphene oxide (GO) solutions homogenously. Moreover, the use of $PMo_{12}$ for *in situ* oxidative polymerization of Py monomer to polypyrrole (PPy) gave a unique structure due to the strong redox ability of $PMo_{12}$.[29,30] Simultaneously, PPy can be decorated on the external surfaces of GO films, whereas $PMo_{12}$ and $Co^{2+}$ ions coated within PPy during the polymerization process. Thus Co–Mo–C/NRGO-1 composite can be obtained with an unchanged morphology from the Co-PCG system. It is worth mentioning that heteroatom-doped carbon materials, particularly the N-dopant, are promising alternatives as electrocatalysts to improve catalytic current density and efficiency. Porous carbon doped with a large amount of N species can be obtained by carbonizing PPy directly. N species also can be partially doped into RGO films at the same time using Co-PCG as precursors. Hitherto, very few metal carbide-based materials have been reported as OER electrocatalysts.[31–33] Unexpectedly, the Co–Mo–C/NRGO-1 composite derived from Co-PCG precursor exhibited a surprisingly high OER and ORR performance as a bi-functional electrocatalyst. In 1 M KOH, Co–Mo–C/NRGO-1 composite presented active OER properties with a low Tafel slope of 42 mV $dec^{-1}$, a small overpotential of 330 mV at a the current density of 10 mA $cm^{-2}$ and long-term stability. To the best of our knowledge, the resulting composite exhibited the highest activity for OER among all the reported carbide-based catalysts. The Co–Mo–C/NRGO-1 also demonstrated good ORR catalytic performance with a positive onset potential of ~−95 mV *vs.* Ag/AgCl, excellent stability for over 30 000 s and methanol tolerance. The excellent catalytic activity towards both OER and ORR can be attributed to the unique structures of Co-PCG precursors and the synergistic effect between active metal/metal carbides and N-doped carbon in Co–Mo–C/NRGO-1 composite.

## Results and discussion

The preparation process of Co–Mo–C/NRGO-1 is illustrated in Scheme 1. Since the PCG system can be synthesized by choosing different POMs and conductive polymer precursors, we first prepared the Co-PCG system using a facile hydrothermal method at 180 °C for 12 h by a simple mixture of $PMo_{12}$, Py, GO films and $Co(NO_3)_2$. In order to synthesize Co–Mo–C/NRGO-1

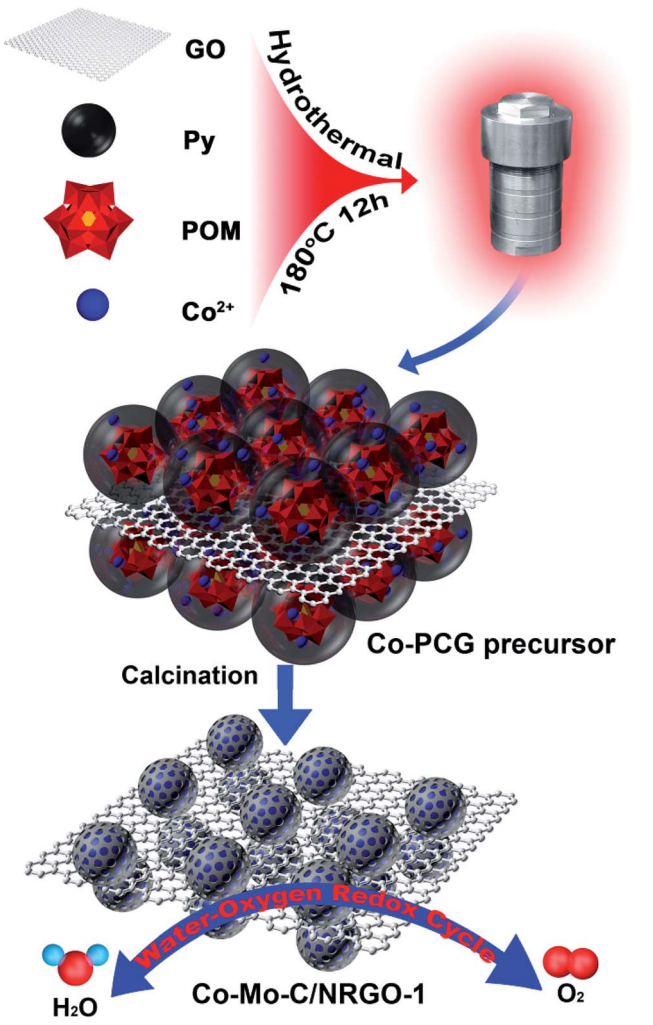


Scheme 1 Schematic of the formation of Co–Mo–C/NRGO-1 composite.

composite, the obtained Co-PCG precursor was carbonized directly in a horizontal tube furnace at 800 °C for 3 h under an $N_2$ atmosphere. Moreover, GO films were reduced to RGO because of the redox ability of POMs and a high pyrolysis temperature. We can also prepare other Co-PCG composites by tailoring the molar ratio of $Co(NO_3)_2$, $PMo_{12}$ and Py monomer (denote as Co-PCG-*n*, $n = 1$–4). Then, PCG-*n* composites were carbonized at 800 °C to get Co–Mo–C/NRGO-*n* ($n = 1$–4) composites. Co–Mo–C/NRGO-1 prepared with different GO concentrations (0–1.6 mg $mL^{-1}$) and different pyrolysis temperatures (700–900 °C) were discussed in the text. On the other hand, $Mo_2C/Co_6Mo_6C_2$/NRGO composite could be obtained with stirring Co–Mo–C/NRGO-1 composite in 5 M HCl solution to remove Co. $Mo_2C$/NRGO could be synthesized from the PCG composite without $Co^{2+}$ doping (see Experimental section). In this study, we selected three composites derived from the Co-PCG-1 and PCG-1 systems at 800 °C (Co–Mo–C/NRGO-1, $Mo_2C/Co_6Mo_6C_2$/NRGO and $Mo_2C$/NRGO) for detailed studies.

The structure of Co–Mo–C/NRGO-1, $Mo_2C/Co_6Mo_6C_2$/NRGO and $Mo_2C$/NRGO were investigated by powder X-ray diffraction (PXRD) first (Fig. 1a). All peaks for the Co–Mo–C/NRGO-1 composite belonged to Co (JCPDS no. 1-1255), $Co_6Mo_6C_2$ (JCPDS no. 80-339) and $Mo_2C$ (JCPDS no. 35-787). After hash acid washing, the Co characteristic peaks of $Mo_2C/Co_6Mo_6C_2$/NRGO disappeared completely. The as-prepared $Mo_2C$/NRGO was just in agreement with $Mo_2C$ card. Moreover, an evident peak at around 26° for the above three samples corresponding to the (002) diffraction peak of graphite carbon was attributed to the presence of RGO and PPy-derived porous carbon. Co–Mo–C/NRGO-1 prepared at different temperatures and Co–Mo–C/NRGO-*n* composites have the same compositions (Fig. S1 and S2†). Then, the morphology of Co–Mo–C/NRGO-1 composite was investigated using scanning electron microscopy (SEM). Because of the heat treatment process, the diameters of the particles for Co–Mo–C/NRGO-1 were smaller than those for Co-PCG composite with similar morphology (Fig. S3†). As can be seen in Fig. 1b, Co–Mo–C/NRGO-1 with sheet-like structures displayed rough surfaces and wrinkled edges because of the uniform polymerization of Py on the external surfaces of the GO films. Fig. 1c is the magnified transmission electron microscopy (TEM) image of Co–Mo–C/NRGO-1, which shows tiny spherical shaped nanoparticles with 2–10 nm diameters. These particles were metal/metal carbides homogenously anchored within N-doped porous carbon, confirming the growth on N-doped RGO sheets. TEM and SEM images of Co–Mo–C/NRGO-*n* composites prepared with different amounts of precursors also can be seen in Fig. S4 and S5.† The TEM and SEM images of $Mo_2C/Co_6Mo_6C_2$/NRGO and $Mo_2C$/NRGO with different compositions showed similar morphologies to Co–Mo–C/NRGO-1 (Fig. S6†). A high-resolution TEM (HRTEM) image (Fig. 1d) could be observed indicating that the crystalline nanoparticles were coated by amorphous carbon during the nucleation process. Importantly, all three types of lattice fringes for Co–Mo–C/NRGO-1 could be found, which are the (110) planes of $Mo_2C$ with the lattice distance of 0.26 nm, the (111) planes of Co with the lattice distance of 0.2 nm and the (422)

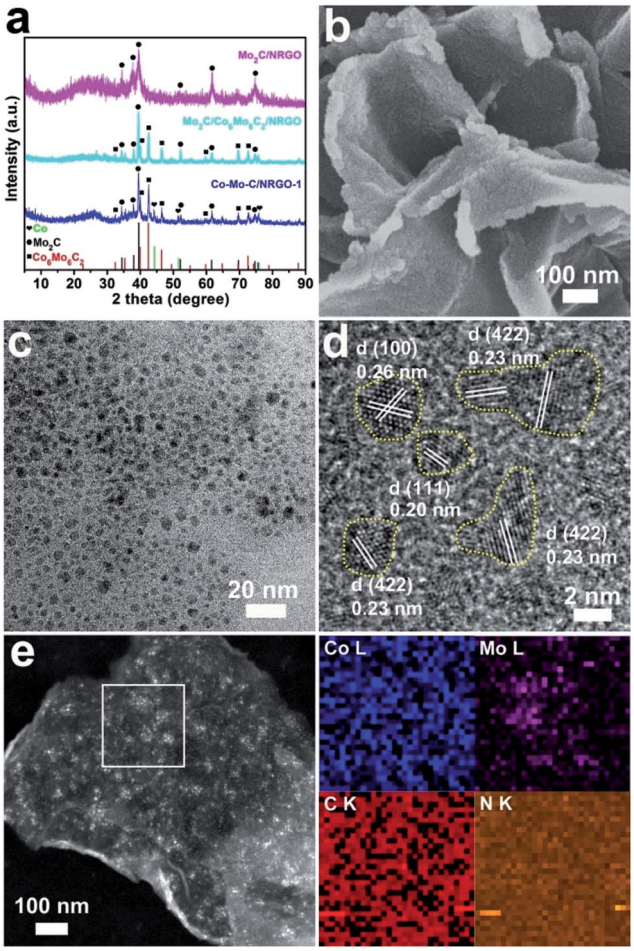


Fig. 1 (a) PXRD patterns of as-prepared samples of Co–Mo–C/NRGO-1, $Mo_2C/Co_6Mo_6C_2$/NRGO, $Mo_2C$/NRGO, respectively. (b and c) SEM and magnified TEM images of Co–Mo–C/NRGO-1 composite. (d) HRTEM image of Co–Mo–C/NRGO-1. (e) HAADF-STEM image of Co–Mo–C/NRGO-1 and the corresponding mappings of Co, Mo, C and N elements, respectively.

planes of $Co_6Mo_6C_2$ with the lattice distance of 0.23 nm, respectively. High-angle annular dark-field scanning TEM (HAADF-STEM) microscopy was used to investigate the elemental distribution of Co–Mo–C/NRGO-1 (Fig. 1e). The corresponding mappings show that Co, Mo, C and N elements could be uniformly detected in the sample, further verifying the formation of Co–Mo–C/NRGO-1. The HRTEM images and mappings for $Mo_2C/Co_6Mo_6C_2$/NRGO and $Mo_2C$/NRGO are also shown in Fig. S7 and S8,† respectively. Moreover, the Co and Mo chemical compositions of Co–Mo–C/NRGO-*n* ($n = 1$–4) were determined using inductively coupled plasma (ICP) analysis (Table S1†) and were in accordance with the ratio of $Co(NO_3)_2$ and $PMo_{12}$ precursors, suggesting the successful preparation of Co–Mo–C/NRGO-1. These results indicated that the morphology control of Co–Mo–C/NRGO-1 could be achieved because of the redox ability and highly dispersion of POMs and the polymerization of Py. Such a structure of small sized particles embedded in a carbon matrix can prevent them from agglomeration and ensure the fast electron transportation efficiently between N-doped carbon and these three types of particles.

 

The chemical states and surface compositions of Co–Mo–C/NRGO-1 composite were characterized by X-ray photoelectron spectroscopy (XPS). As can be seen in Fig. 2a, the XPS spectrum of Co–Mo–C/NRGO-1 reveals the composition of C (62.7 at%), N (16.4 at%), Mo (4.6 at%), Co (1.2 at%), O (14.5 at%) and a little of P (0.4 at%) derived from $PMo_{12}$, confirming that Co was successfully doped into the PCG system. Energy dispersive X-ray spectrometry (EDX) of Co–Mo–C/NRGO-1 (Fig. S9†) also detected all these elements. The decomposed Co2p spectrum (Fig. 2b) shows two prominent peaks at 796.4 eV and 780.7 eV, which were assigned to $Co2p_{1/2}$ and $Co2p_{3/2}$, respectively. The difference of binding energy between $Co2p_{1/2}$ and $Co2p_{3/2}$ was approximately 15.6 eV, which demonstrated the presence of $Co^{2+}$ and $Co^{3+}$ species in the Co–Mo–C/NRGO-1 composite.[34] Two weak 2p satellite peaks could also be observed at 804.1 eV and 786.4 eV binding energies. The Co2p binding energies are coincident with pure Co and Co-based carbides, and therefore they could not be distinguished clearly.[35] The Mo3d spectrum (Fig. 2c) reveals the +4 oxidation state of Mo ($Mo3d_{3/2}$ at 232.1 eV and $Mo3d_{5/2}$ at 228.5 eV), which was assigned to the formation of Mo-based carbides including $Co_6Mo_6C_2$ and $Mo_2C$. The +6 oxidation state of Mo observed at 235.7 eV ($Mo3d_{3/2}$) and 232.8 eV ($Mo3d_{5/2}$) may be attributed to the oxidation of the samples due to air exposure.[29] Fig. 2d is the high-resolution C1s spectrum, which shows the main graphite-like carbon bond (C–C/C=C) at 284.4 eV, C–N bond at 285.1 eV along with C–O bond at 286.6 eV, proving that N species were doped into the carbon lattice. The high-resolution N1s spectrum (Fig. 2e) could be deconvoluted into four peaks, which were assigned to graphitic N (400.3 eV), pyrrolic N (398.8 eV), pyridinic N (397.7 eV) and Mo3p (394.5 eV). The Mo3p peak is related to the Mo–N bond, suggesting the partial Mo bonding with the N species of the PPy-derived porous carbon. According to peak area of different N species (Table S2†), the amounts of pyridinic N were determined to be 49.8%. Such a high proportion of pyridinic N can lead to enhanced intrinsic electrochemical activity, thus boosting the OER and ORR performance for Co–Mo–C/NRGO-1 composite greatly.[36,37] The O1s spectrum (Fig. 2f) shows the main peak at 530.5 eV, a value typical for C–O/O=C bonds, whereas the other two peaks at 531.4 eV and 532.3 eV are for N–C–O bonds and chemisorbed oxygen. These XPS data further confirm the formation of the Co–Mo–C/NRGO-1 composite. Compared with Co–Mo–C/NRGO-1 composite, $Mo_2C/Co_6Mo_6C_2$/NRGO composite showed an apparent decrease in both Co composition and the intensity of the Co2p spectrum, which proves the removal of Co (Fig. S10†). XPS spectra of $Mo_2C$/NRGO composite are shown in Fig. S11.†

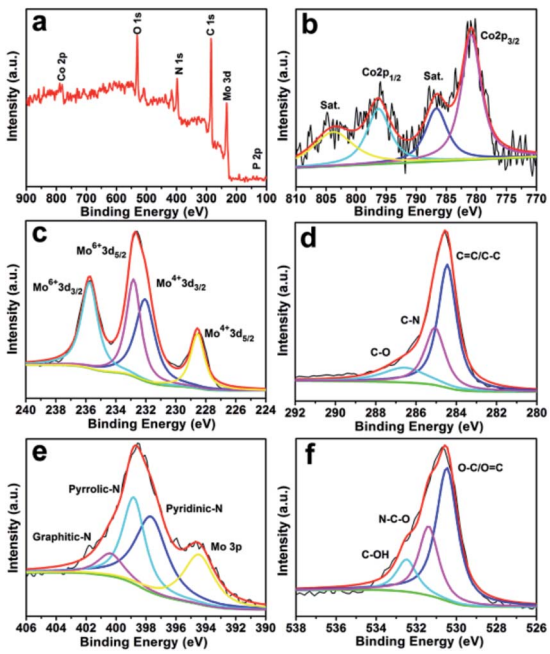


Fig. 2 (a) XPS spectrum of Co–Mo–C/NRGO-1 composite. (b) Co2p, (c) Mo3d, (d) C1s, (e) N1s and (f) O1s high-resolution XPS spectra.

Raman spectra of Co–Mo–C/NRGO-1 composite prepared with different amounts of GO precursors (0, 1.0 and 1.6 mg $mL^{-1}$) all exhibited significant D bands located around 1365.6 $cm^{-1}$ and G bands around 1597.8 $cm^{-1}$ (Fig. S12†). In general, the D and G bands represent the $sp^3$ defect sites and $sp^2$-bonded pairs, respectively, which are used to study the degree of graphitization. The $I_D/I_G$ ratio of Co–Mo–C/NRGO-1 composite (1.0 mg $mL^{-1}$ GO) was 0.88, suggesting a high degree of graphitization. Fig. S13a† shows the $N_2$ adsorption/desorption isotherms of the main three samples. Using the Brunauer–Emmett–Teller (BET) method, Co–Mo–C/NRGO-1 composite presented the largest BET surface area (124.6 $m^2$ $g^{-1}$), whereas the BET surface areas of $Mo_2C/Co_6Mo_6C_2$/NRGO and $Mo_2C$/NRGO were 114.3 and 80.6 $m^2$ $g^{-1}$, respectively. The corresponding pore size distributions calculated from the Barrett–Joyner–Halenda (BJH) model (Fig. S13b†) indicated a high portion of mesopores.

The OER performance of Co–Mo–C/NRGO-1 composite was determined in a standard three-electrode cell setup with an $N_2$-saturated 1 M KOH electrolyte by depositing catalysts onto a glassy carbon (GC) electrode (see the Experimental section). The ohmic potential drop (*IR*) from the solution resistance was corrected for all polarization curves (Fig. S14†). First, Co–Mo–C/NRGO-*n* composites prepared with different Co/Mo molar ratios and Py monomer precursors were tested to select the optimal conditions for OER, that is Co–Mo–C/NRGO-1 (Fig. S15†). Co–Mo–C/NRGO-1 catalysts prepared at different carbonization temperatures and with different GO films were also measured for comparison (Fig. S16 and S17†). In contrast, $Mo_2C/Co_6Mo_6C_2$/NRGO, $Mo_2C$/NRGO and commercial $IrO_2$ were also measured under the same conditions. As can be seen from Fig. 3a, the linear sweep voltammetry (LSV) curve of Co–Mo–C/NRGO-1 showed an earlier onset potential of ~1.51 V *vs.* RHE and a dramatically increased kinetic current, whereas commercial $IrO_2$ had a more negative onset potential (~1.48 V *vs.* RHE) but poor OER current. The OER activity of Co–Mo–C/NRGO-1 was also higher than that of the as-prepared $Mo_2C/Co_6Mo_6C_2$/NRGO and $Mo_2C$/NRGO samples. The overpotential achieved for a current density of 10 mA $cm^{-2}$ ($\eta_{10}$) is a desirable OER parameter in solar fuel synthesis.[14,38] Outstandingly, the $\eta_{10}$ of the Co–Mo–C/NRGO-1 catalyst was only 330 mV (compared with the 1.23 V standard reaction potential), which is much smaller than that of $Mo_2C/Co_6Mo_6C_2$/NRGO (360 mV) and

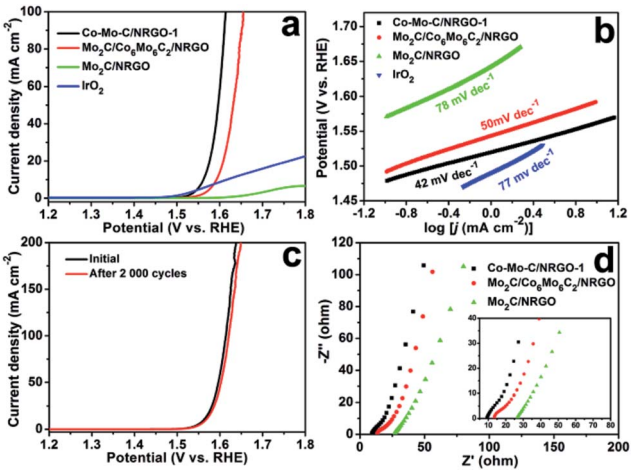


Fig. 3 (a) LSV curves of Co–Mo–C/NRGO-1, $Mo_2C/Co_6Mo_6C_2$/NRGO, $Mo_2C$/NRGO and $IrO_2$ with a 5 mV $s^{-1}$ scan rate for OER. (b) The corresponding Tafel plots derived from (a). (c) LSV curves of Co–Mo–C/NRGO-1 before and after 2000 CV cycles stability test. (d) Nyquist plots of corresponding catalysts tested at the open circuit potential. All experiments were carried out in 1 M $O_2$-saturated KOH electrolyte.

the commercial $IrO_2$ (387 mV). The Tafel plots of the above four catalysts for OER can be observed in Fig. 3b. At relatively lower overpotential regions, Co–Mo–C/NRGO-1 had a very small 42 mV $dec^{-1}$ Tafel slope, whereas the Tafel slopes of $Mo_2C/Co_6Mo_6C_2$/NRGO, $Mo_2C$/NRGO and $IrO_2$ were 50, 78 and 77 mV $dec^{-1}$, respectively. Notably, Co–Mo–C/NRGO-1 composite owned the smallest Tafel slope, even lower than commercial state-of-art $IrO_2$, which suggests excellent intrinsic kinetics for OER performance. The OER activity of Co–Mo–C/NRGO-1 catalyst is comparable and even superior to recently reported Co-based materials, such as $Co_3O_4$/N-rmGO,[39] CoMn LDH,[40] (Co-NMC)$_1$/NC[41] and Co–P[42] (Table S3†). Moreover, either the $\eta_{10}$ or the Tafel plot of Co–Mo–C/NRGO-1 catalyst for OER performance in alkaline medium is the smallest among all the reported carbide-based OER catalysts (Table 1).

Long-term stability is another important parameter to determine the practicality of the OER electrocatalysts. The LSV curves were conducted before and after the potential sweeps from 1.4 V to 1.6 V *vs.* RHE for 2000 CV cycles. As shown in Fig. 3c, after 2000 cycles, the polarization curve of Co–Mo–C/NRGO-1 almost overlaps with the initial one. The $\eta_{10}$ value only had a differential of ~1 mV increase after 2000 CV cycles, suggesting the superior durability of Co–Mo–C/NRGO-1 composite. In addition, the water oxidation activity also depended largely on the electrochemical active surface area (ECSA) of the solid–liquid interface for electrocatalysts, which can be estimated by the double layer capacitance ($C_{dll}$). In Fig. S18,† $C_{dll}$ value of Co–Mo–C/NRGO-1, $Mo_2C/Co_6Mo_6C_2$/NRGO and $Mo_2C$/NRGO catalysts are 16.3, 6.2 and 0.4 mF $cm^{-2}$, respectively, which are in accordance with their OER performance. Therefore, Co–Mo–C/NRGO-1 catalyst with the largest $C_{dll}$ value possesses increased ECSA because of the rougher surface achieved during the carbonization, which implies that the morphology and structure of the electrocatalyst play a key role in the OER activity.

Electrochemical impedance spectroscopy (EIS) measurements were also performed to reveal the OER kinetics on the electrode/electrolyte surface of the three abovementioned samples, as shown in Fig. 3d. The charge transfer resistance ($R_{ct}$) of Co–Mo–C/NRGO-1 catalyst fitted according to the high-frequency semicircle was only 9.4 Ω, which is much smaller than $Mo_2C/Co_6Mo_6C_2$/NRGO (17.1 Ω) and $Mo_2C$/NRGO (43.8 Ω). Furthermore, Co–Mo–C/NRGO-1 catalyst exhibited a vertical slope of the linear part in the low-frequency region, which suggests rapid ion diffusion and electron transfer. Such a low $R_{ct}$ value of Co–Mo–C/NRGO-1 indicates that the fast ion penetration and charge transfer kinetics on the surface of the catalyst might be caused by the active nanoparticles embedded in N-doped carbon and RGO films.

The ORR electrocatalytic activities of Co–Mo–C/NRGO-1, $Mo_2C/Co_6Mo_6C_2$/NRGO, $Mo_2C$/NRGO and commercial 20% Pt/C catalysts were recorded using rotating disk electrode (RDE) measurements in 0.1 M $O_2$-saturated KOH electrolytes. As shown in Fig. 4a, the polarization curve of Co–Mo–C/NRGO-1 obtained on RDE at a rotation rate of 1600 rpm showed an onset potential around −95 mV *vs.* Ag/AgCl and half-wave potential around −178 mV *vs.* Ag/AgCl, which were closer to the activity of commercial 20% Pt/C catalyst and higher than that of $Mo_2C/Co_6Mo_6C_2$/NRGO and $Mo_2C$/NRGO catalysts. The cyclic voltammetry (CV) curves of Co–Mo–C/NRGO-1 in $N_2$- and $O_2$-saturated electrolytes are shown in Fig. S19a.† A quasi-rectangular CV

Table 1 Comparison of OER performance for relevant electrocatalysts in this study and other carbide-based electrocatalysts in an alkaline electrolyte

| Sample | Loadings (mg $cm^{-2}$) | Electrolyte | Tafel slope (mV $dec^{-1}$) | $\eta_{10}$[a] (mV) | Reference |
|---|---|---|---|---|---|
| Co–Mo–C/NRGO-1 | ~0.14 | 1 M KOH | 42 | 330 | This study |
| $Mo_2C/Co_6Mo_6C_2$/NRGO | ~0.14 | 1 M KOH | 50 | 360 | This study |
| $Mo_2C$/NRGO | ~0.14 | 1 M KOH | 78 | — | This study |
| $IrO_2$ | ~0.14 | 1 M KOH | 77 | 387 | This study |
| $Fe_3C$@NG800–0.2 | ~0.20 | 0.1 M KOH | 62 | 361 | 31 |
| $Co_3ZnC$/Co@CN | 0.344 | 1 M KOH | 81 | 366 | 32 |
| Fe/$Fe_3C$@N-graphite layer | 0.7 | 0.1 M KOH | — | 770 | 33 |

[a] Overpotential reported with respect to RHE.

 

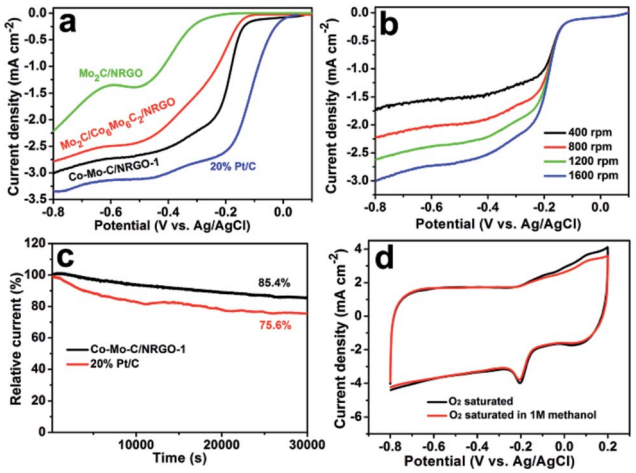


Fig. 4 (a) LSV curves of Co–Mo–C/NRGO-1, $Mo_2C/Co_6Mo_6C_2$/NRGO, $Mo_2C$/NRGO and 20% Pt/C catalysts in $O_2$-saturated 0.1 M KOH with a scan rate of 5 mV $s^{-1}$ and a rotation speed of 1600 rpm. (b) LSV curves of Co–Mo–C/NRGO-1 at different rotation rates. (c) Chronoamperometry curves of Co–Mo–C/NRGO-1 and 20% Pt/C catalysts with constant potential at −0.3 V *vs.* Ag/AgCl and a rotation speed of 1600 rpm for 30 000 s. (d) CV curves of Co–Mo–C/NRGO-1 in 0.1 M KOH without and with 1 M MeOH.

curve without any redox peak was obtained in $N_2$-saturated electrolyte. CV curves tested in $O_2$-saturated electrolyte displayed a prominent cathodic peak at −0.22 V *vs.* Ag/AgCl, indicating outstanding ORR catalytic activity. To analyze the kinetic parameters of Co–Mo–C/NRGO-1 composite, the Koutecky–Levich (K–L) equation was also used to evaluate the electron transfer number ($n$) according to the LSV curves of Co–Mo–C/NRGO-1 at different rotation rates (Fig. 4b and S19b†). The K–L plots for Co–Mo–C/NRGO-1 showed good linearity and the slopes were kept almost constant over the potential from −0.4 to −0.8 V *vs.* Ag/AgCl, which indicated the concentration of dissolved oxygen with first-order reaction kinetics.[39,43] The $n$ was 3.1 at −0.8 V *vs.* Ag/AgCl according to the slopes of K–L plots, suggesting a two-step two-electron reduction process with $H_2O_2$ intermediate for the incomplete reduction of oxygen on the Co–Mo–C/NRGO-1 catalyst. The long-term stability for ORR is also an important parameter in alkaline fuel cell technology.[44] The chronoamperometry curves for Co–Mo–C/NRGO-1 and 20% Pt/C are shown in Fig. 4c. It is worth noting that Co–Mo–C/NRGO-1 retained 85.4% of the initial current after 30 000 s of testing, whereas 20% Pt/C catalyst retained only 75.6%. Such good durability of Co–Mo–C/NRGO-1 may be due to the unique structure of locally crystallized metal/metal carbides embedded in N-doped carbon and RGO films. Furthermore, the tolerance of methanol property can be measured by injecting 1 M MeOH into the electrolyte. In Fig. 4d, CV curves of Co–Mo–C/NRGO-1 before and after injecting 1 M MeOH into $O_2$-saturated 0.1 M KOH electrolyte showed almost no change of cathodic current, indicating excellent tolerance to MeOH crossover. All these results proved that Co–Mo–C/NRGO-1 composite possessed robust catalytic sites and excellent ORR performance.

Based on the abovementioned structural and compositional discussions of the Co–Mo–C/NRGO-1 composite, such superior OER and ORR performance could be attributed to the following important aspects. First, the synergistic effects among Co, $Co_6Mo_6C_2$, $Mo_2C$, N-doped carbon and N-doped RGO improve the OER and ORR performance. Second, thermal reduction of GO into RGO and carbonization of PPy into amorphous carbon during the annealing process can increase the electrical conductivity and surface area of the Co–Mo–C/NRGO-1 composite thus leading to better OER and ORR catalytic activity. Third, high content of nitrogen, particularly pyridinic N, doped into PPy-derived porous carbon and RGO films provide more active sites that can increase the electrochemical current density and enhance the hydrophilicity to strikingly accelerate the electrolyte–electrode interaction. Furthermore, using Co-PCG as a sacrificial precursor is beneficial to obtain such unique nanostructured carbides and graphene-based composite, which has high dispersion of metal/metal carbides nanoparticles coated within N-doped porous carbon and RGO films. Altogether, all these factors have demonstrated the advantages of using the Co-PCG precursor for the synthesis of an excellent bi-functional Co–Mo–C/NRGO-1 electrocatalyst.

## Conclusions

In summary, a highly efficient Co–Mo–C/NRGO-1 electrocatalyst derived from a Co-doped PCG precursor was synthesized using a facile two-step strategy. The catalytic performance of the as-prepared electrocatalyst for both OER and ORR in alkaline electrolyte was investigated because the platform of the remarkable Co-PCG precursors could be employed for preparing the desired products. Co–Mo–C/NRGO-1 composite showed the highest OER performance among all the carbide-based electrocatalysts in the alkaline electrolyte with the Tafel slope of 42 mV $dec^{-1}$, $\eta_{10}$ of 330 mV and long-term stability. The ORR performance was also nontrivial, which showed outstanding durability and superior methanol tolerance. Both the conspicuous structures of Co-PCG precursor and the synergetic effects between metal/metal carbides and N-doped RGO ensured excellent OER and ORR performance. Our study presents a great prospect to design and synthesize hybrid materials with unique structures using a suitable PCG system as a precursor for developing a water–oxygen redox cycle system and has a potential to act as multifunctional catalysts for other energy conversion and storage.

## Acknowledgements

This work was financially supported by NSFC (No. 21622104, 21371099 and 21471080), the NSF of Jiangsu Province of China (No. BK20130043 and BK20141445), the Priority Academic Program Development of Jiangsu Higher Education Institutions, and the Foundation of Jiangsu Collaborative Innovation Center of Biomedical Functional Materials.

## Notes and references

1 H. B. Gray, *Nat. Chem.*, 2009, **1**, 7.
2 N. S. Lewis, *Science*, 2007, **315**, 798–801.
3 M. W. Kanan, Y. Surendranath and D. G. Nocera, *Chem. Soc. Rev.*, 2009, **38**, 109–114.
4 M. Winter and R. J. Brodd, *Chem. Rev.*, 2004, **104**, 4245–4270.
5 M. G. Walter, E. L. Warren, J. R. McKone, S. W. Boettcher, Q. Mi, E. A. Santori and N. S. Lewis, *Chem. Rev.*, 2010, **110**, 6446–6473.
6 K. Maeda, K. Teramura, D. Lu, T. Takata, N. Saito, Y. Inoue and K. Domen, *Nature*, 2006, **440**, 295.
7 Y. Lee, J. Suntivich, K. J. May, E. E. Perry and Y. Shao-Horn, *J. Phys. Chem. Lett.*, 2012, **3**, 399–404.
8 V. Stamenkovic, B. S. Mun, K. J. J. Mayrhofer, P. N. Ross, N. M. Markovic, J. Rossmeisl, J. Greeley and J. K. Nørskov, *Angew. Chem., Int. Ed.*, 2006, **118**, 2963–2967.
9 D. Chen, C. Chen, Z. M. Baiyee, Z. Shao and F. Ciucci, *Chem. Rev.*, 2015, **115**, 9869–9921.
10 Y. Gorlin and T. F. Jaramillo, *J. Am. Chem. Soc.*, 2010, **132**, 13612–13614.
11 S. Mao, Z. Wen, T. Huang, Y. Hou and J. Chen, *Energy Environ. Sci.*, 2014, **7**, 609–616.
12 J. Wang, W. Cui, Q. Liu, Z. Xing, A. M. Asiri and X. Sun, *Adv. Mater.*, 2016, **28**, 215–230.
13 D. U. Lee, P. Xu, Z. P. Cano, A. G. Kashkooli, M. G. Park and Z. Chen, *J. Mater. Chem. A*, 2016, **4**, 7107–7134.
14 C. C. L. McCrory, S. Jung, J. C. Peters and T. F. Jaramillo, *J. Am. Chem. Soc.*, 2013, **135**, 16977–16987.
15 Y. N. Regmi, G. R. Waetzig, K. D. Duffee, S. M. Schmuecker, J. M. Thode and B. M. Leonard, *J. Mater. Chem. A*, 2015, **3**, 10085–10091.
16 H. H. Hwu and J. G. Chen, *Chem. Rev.*, 2005, **105**, 185–212.
17 M. Naguib, O. Mashtalir, J. Carle, V. Presser, J. Lu, L. Hultman, Y. Gogotsi and M. W. Barsoum, *ACS Nano*, 2012, **6**, 1322–1331.
18 H. Vrubel and X. Hu, *Angew. Chem., Int. Ed.*, 2012, **124**, 12875–12878.
19 C. Wan, Y. N. Regmi and B. M. Leonard, *Angew. Chem., Int. Ed.*, 2014, **126**, 6525–6528.
20 W.-F. Chen, J. T. Muckerman and E. Fujita, *Chem. Commun.*, 2013, **49**, 8896–8909.
21 W. F. Chen, C. H. Wang, K. Sasaki, N. Marinkovic, W. Xu, J. T. Muckerman, Y. Zhu and R. R. Adzic, *Energy Environ. Sci.*, 2013, **6**, 943–951.
22 X. Ma, H. Meng, M. Cai and P. K. Shen, *J. Am. Chem. Soc.*, 2012, **134**, 1954–1957.
23 Y. Liu, G.-D. Li, L. Yuan, L. Ge, H. Ding, D. Wang and X. Zou, *Nanoscale*, 2015, **7**, 3130–3136.
24 P. Xiao, X. Ge, H. Wang, Z. Liu, A. Fisher and X. Wang, *Adv. Funct. Mater.*, 2015, **25**, 1520–1526.
25 H. Wang, T. Maiyalagan and X. Wang, *ACS Catal.*, 2012, **2**, 781–794.
26 Z. Lin, G. H. Waller, Y. Liu, M. Liu and C.-P. Wong, *Carbon*, 2013, **53**, 130–136.
27 Y. Chen, M. Han, Y. Tang, J. Bao, S. Li, Y. Lan and Z. Dai, *Chem. Commun.*, 2015, **51**, 12377–12380.
28 J.-S. Li, Y. Wang, C.-H. Liu, S.-L. Li, Y.-G. Wang, L.-Z. Dong, Z.-H. Dai, Y.-F. Li and Y.-Q. Lan, *Nat. Commun.*, 2016, **7**, 11204–11212.
29 Y.-J. Tang, Y. Wang, X.-L. Wang, S.-L. Li, W. Huang, L.-Z. Dong, C.-H. Liu, Y.-F. Li and Y.-Q. Lan, *Adv. Energy Mater.*, 2016, **6**, 160016–160022.
30 C. R. Martin, *Acc. Chem. Res.*, 1995, **28**, 61–68.
31 H. Jiang, Y. Yao, Y. Zhu, Y. Liu, Y. Su, X. Yang and C. Li, *ACS Appl. Mater. Interfaces*, 2015, **7**, 21511–21520.
32 J. Su, G. Xia, R. Li, Y. Yang, J. Chen, R. Shi, P. Jiang and Q. Chen, *J. Mater. Chem. A*, 2016, **4**, 9204–9212.
33 B. K. Barman and K. K. Nanda, *Green Chem.*, 2016, **18**, 427–432.
34 L. Fu, Z. Liu, Y. Liu, B. Han, P. Hu, L. Cao and D. Zhu, *Adv. Mater.*, 2005, **17**, 217–221.
35 X.-H. Wang, M.-H. Zhang, W. Li and K.-Y. Tao, *Dalton Trans.*, 2007, 5165–5170.
36 K. Gong, F. Du, Z. Xia, M. Durstock and L. Dai, *Science*, 2009, **323**, 760–764.
37 J. Liang, Y. Jiao, M. Jaroniec and S. Z. Qiao, *Angew. Chem., Int. Ed.*, 2012, **51**, 11496–11500.
38 C. C. L. McCrory, S. Jung, I. M. Ferrer, S. M. Chatman, J. C. Peters and T. F. Jaramillo, *J. Am. Chem. Soc.*, 2015, **137**, 4347–4357.
39 Y. Liang, Y. Li, H. Wang, J. Zhou, J. Wang, T. Regier and H. Dai, *Nat. Mater.*, 2011, **10**, 780–786.
40 F. Song and X. Hu, *J. Am. Chem. Soc.*, 2014, **136**, 16481–16484.
41 B. Bayatsarmadi, Y. Zheng, Y. Tang, M. Jaroniec and S.-Z. Qiao, *Small*, 2016, **12**, 3703–3711.
42 N. Jiang, B. You, M. Sheng and Y. Sun, *Angew. Chem., Int. Ed.*, 2015, **54**, 6251–6254.
43 K. J. J. Mayrhofer, D. Strmcnik, B. B. Blizanac, V. Stamenkovic, M. Arenz and N. M. Markovic, *Electrochim. Acta*, 2008, **53**, 3181–3188.
44 X. Yu and S. Ye, *J. Power Sources*, 2007, **172**, 145–154.

 